Nonlocal Superconducting Single-Photon Detector

Federico Paolucci*

Istituto Nazionale Fisica Nucleare (INFN) Sezione di Pisa, Largo Bruno Pontecorvo 3, Pisa I-56127, Italy

(Received 24 March 2023; revised 9 June 2023; accepted 12 June 2023; published 5 July 2023)

We present and theoretically analyze the performance of a *nonlocal* superconducting single-photon detector. The device operates due to the *energy-to-phase* conversion mechanism, where the energy of the absorbed single photon is transformed in a variation of the superconducting phase. Within this scope, the detector is designed in the form of a double-loop superconductor–normal-metal–superconductor (*S*-*N*-*S*) Josephson interferometer, where the detection occurs in a *long S*-*N*-*S* junction and the readout is operated by a *short S*-*N*-*S* junction. The variation of the superconducting phase across the readout junction is measured by recording the quasiparticle current flowing through a tunnel-coupled superconducting probe. By exploiting realistic geometry and materials, the detector is able to reveal single photons of frequency down to 10 GHz when operated at 10 mK. Furthermore, the device provides a value of the signal-to-noise ratio of up 10^4 in the range from 10 GHz to 10 THz by selection of the magnetic flux and the bias voltage. This device will hopefully find direct application as a single-photon detector in both basic science and quantum technology, while the energy-to-phase conversion mechanism could be the basis of nonlocal readout and memory architectures for superconducting qubits.

DOI: 10.1103/PhysRevApplied.20.014003

I. INTRODUCTION

Superconducting local detectors are the state of the art for sensing electromagnetic radiation of energies ranging from hundreds of kiloelectronvolts (x rays) to tens of microelectronvolts (approximately 10 GHz). In particular, superconductivity is exploited to boost the sensitivity of both bolometers and calorimeters operating at the lower frequency boundary. Indeed, the most-used superconducting detectors in the gigahertz-terahertz band are the transition-edge sensors (TESs) [1] and the kinetic inductance detectors (KIDs) [2], due to their extreme sensitivity and robustness. TES bolometers have reached a noise-equivalent power (NEP) on the order of 10^{-19} W/Hz$^{1/2}$ [3], while KIDs have shown an NEP of approximately 10^{-18} W/Hz$^{1/2}$ [4]. Moreover, these structures have shown a frequency resolution of several hundreds of gigahertz when operated as single-photon detectors [5,6]. To push detection technology toward higher sensitivities and lower frequencies, miniaturization of the sensing element has been proposed [7]. Indeed, superconducting-nanowire single-photon detectors (SNSPDs) have been developed in the visible and infrared bands by exploiting quasi-one-dimensional channels [8,9]. Furthermore, the Josephson effect in hybrid superconducting nanostructures is a fundamental element in the design of radiation sensors and improvement of the detection sensitivity. Indeed, single-photon counters based on tunnel Josephson junctions working down to a few tens of gigahertz [10,11], ultrasensitive proximity nanobolometers [12,13], thermoelectric calorimeters [14,15], and the current-tunable Josephson escape sensor (JES) [16] have been designed and realized. On the one hand, the strong temperature dependence of superconductivity increases the sensitivity of a detector. On the other hand, a local readout operation performed directly on the sensing element could alter the detection, due to the introduction of even a small amount of overheating. To avoid this drawback, a *nonlocal* architecture separating the detector and the readout element can be beneficial. Within this scope, detectors exploiting temperature-to-phase conversion (TPC) [17] and temperature-to-voltage conversion (TVC) [18] have been proposed.

Here, we propose a nonlocal superconducting single-photon detector based on the energy-to-phase conversion mechanism, which is expected to show improved performance with respect to existing superconducting sensors. To this end, we exploit a double-loop Josephson interferometer [19,20], where the absorption of a single photon in a *long* superconductor–normal-metal–superconductor (*S*-*N*-*S*) Josephson junction (detector) causes the variation of the superconducting phase across a *short S*-*N*-*S* junction (readout). The output signal is obtained by measuring the quasiparticle current flowing through a tunnel probe coupled directly to the readout junction. The double-loop geometry and the asymmetry between

*federico.paolucci@pi.infn.it

the two junctions (detector and readout) ensure optimal energy-to-phase conversion, thus boosting the detection sensitivity. Indeed, our detector is expected to efficiently reveal single photons of frequency down to 10 GHz. Differently from other superconducting devices, the proposed detector can be tuned *in situ* by controlling both the magnetic flux piercing the interferometer and the bias voltage.

The paper is organized as follows. In Sec. II, the device structure and its operation principle are introduced; in Sec. III, the geometrical dimensions and the materials constituting each element of the structure are listed; in Sec. IV, the effects of photon absorption on the electronic temperature of the detector junction are shown; in Sec. V, the energy-to-phase conversion and its effects on the energy spectrum of the *S*-*N*-*S* readout junction are evaluated; in Sec. VI, the dependence of the output current on the photon frequency is shown; in Sec. VII, the detection performance of the device is displayed; and in Sec. VIII, the concluding remarks are presented.

II. OPERATION PRINCIPLE AND STRUCTURE

The structure of our single-photon detector is shown in Fig. 1(a), where a *long*-detection *S*-*N*-*S* junction (d, red) is integrated in a two-loop Josephson interferometer (gray) together with a *short*–*S*-*N*-*S*–readout Josephson junction (r, orange). Then, a superconducting probe (p, blue) is tunnel coupled directly to r. The device operation is based on the strong temperature dependence of the supercurrent flowing in d, since it is in the *long*-junction limit [21]. Indeed, the current-to-phase relation (CPR) of d can be written as

$$I_d(T_d,\varphi_d) = I_{C,d}(T_d)\sin(\varphi_d), \tag{1}$$

where $I_{C,d}$ is the critical current of the junction, T_d is the electron temperature of d, and φ_d is the superconducting phase drop across the junction. The absorption of a single photon causes the increase of T_d (for details, see Sec. IV) and, thus, exponential damping of the critical current of d [22,23]

$$I_{C,d}(T_d) = \frac{64\pi k_B T_d}{(3+2\sqrt{2})eR_d} \times \sqrt{\frac{2\pi k_B T_d}{E_{\mathrm{th},d}}}\exp\left(-\sqrt{\frac{2\pi k_B T_d}{E_{\mathrm{th},d}}}\right), \tag{2}$$

where e is the electron charge, k_B is the Boltzmann constant, R_d is the normal-state resistance of the junction, $E_{\mathrm{th},d} = \hbar D_d/\mathcal{L}_d^2$ is the Thouless energy (in which $\hbar$ is the reduced Planck constant, D_d is the diffusion coefficient, and $\mathcal{L}_d$ is the length of the proximitized normal-metal strip). Since d is inserted in a superconducting loop, it is subject to fluxoid quantization

$$\varphi_d + \frac{2\pi L_d}{\Phi_0} I_{\mathrm{tot}} = \frac{2\pi\Phi_d}{\Phi_0}, \tag{3}$$

where L_d is the inductance of the detection loop, $I_{\mathrm{tot}} = I_d + I_r$ (in which I_r is the switching current of the readout junction) is the total supercurrent circulating in the detector, Φ_d is the magnetic flux bias, and Φ_0 is the flux quantum. Since I_d (and thus I_{tot}) strongly depends on the electronic temperature of d, the increase of T_d due to the absorption of a single photon of energy $h\nu$ (in which h is the Planck constant and ν is the photon frequency) causes a variation of φ_d. Therefore, our single-photon detector operates due to *energy-to-phase* conversion.

The *nonlocal* readout is guaranteed by the second superconducting loop, which is assumed to be fully screened from the external magnetic flux ($\Phi_r = 0$). Consequently, the phase drop across r (φ_r) is linked to φ_d by

$$\varphi_r - \varphi_d + \frac{2\pi L_r}{\Phi_0} I_r = 0, \tag{4}$$

where L_r is the inductance of the readout loop. Thus, the absorption of a single photon by d indirectly produces the variation of φ_r (for details, see Sec. V). The typical method to record a phase variation in an *S*-*N*-*S* junction is tunnel spectroscopy of the normal-metal island, thus implementing a superconducting quantum interference proximity transistor (SQUIPT) [24]. The choice of r in the short-junction limit ensures the maximum response to changes of φ_r and thus of its density of states (DOS) [25]. Within this assumption, the CPR of r takes the Kulik-Omel'yanchuk (KO) form [26]

$$I_r(T_r,\varphi_r) = \frac{\pi\Delta(T_r)}{eR_r}\cos\left(\frac{\varphi_r}{2}\right) \times \int_{\Delta(T_r)\cos\left(\frac{\varphi_r}{2}\right)}^{\Delta(T_r)} \mathrm{d}\varepsilon\, \frac{\tanh\left(\frac{\varepsilon}{k_B T_r}\right)}{\sqrt{\varepsilon^2 - \Delta^2(T_r)\cos^2\left(\frac{\varphi_r}{2}\right)}}, \tag{5}$$

where $\Delta(T_r)$ is the temperature-dependent energy gap of the ring, R_r is the normal-state resistance of r, and ε is the energy relative to the chemical potential of the superconductor. Accordingly, φ_r strongly influences the DOS of the normal-metal stripe ($\mathcal{N}_r$) forming the readout junction

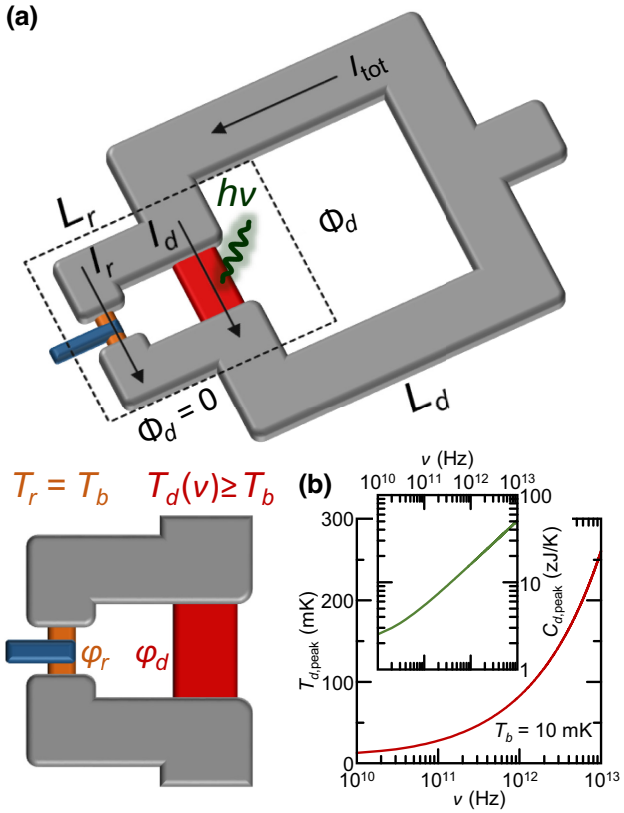

FIG. 1. (a) A schematic of the nonlocal superconducting single-photon detector. The device is structured as a long-detection (d with phase φ_d, red) and short-readout (r with phase φ_r, orange) S-N-S Josephson junction interrupting two superconducting loops (gray) of inductance L_d and L_r, respectively. The total circulating current ($I_{\rm tot}$) divides between d (with switching current I_d) and r (with switching current I_r). The first loop is pierced by a magnetic flux Φ_d, while the readout loop is fully screened from the external magnetic field ($\Phi_r = 0$). A superconducting output probe (blue) is tunnel coupled to r. (b) The peak temperature of the detection junction ($T_{d,\rm peak}$) versus the frequency (ν). The inset shows the thermal capacitance of d versus ν calculated at the peak temperature. All calculations are performed for $T_b = 10$ mK.

[27,28]

$$\mathcal{N}_r(x,\varepsilon,\varphi_r) = \mathrm{Re}\Bigg[\sqrt{\frac{(\varepsilon+i\Gamma_r)^2}{(\varepsilon+i\Gamma_r)^2-\Delta^2(T_r)\cos^2(\frac{\varphi_r}{2})}} \times \cosh\left(\frac{2x-\mathcal{L}_r}{\mathcal{L}_r}\mathrm{arccosh}\sqrt{\frac{(\varepsilon+i\Gamma_r)^2-\Delta^2(T_r)\cos^2(\frac{\varphi_r}{2})}{(\varepsilon+i\Gamma_r)^2-\Delta^2(T_r)}}\right)\Bigg], \quad (6)$$

where Γ_r is the Dynes broadening parameter [29] and $x \in [0, \mathcal{L}_r]$ is the spatial coordinate along r. Furthermore, the superconducting minigap induced by the proximity effect is written as [30]

$$E_{g,r}(T_r,\varphi_r) = \Delta(T_r)\cos\left(\frac{\varphi_r}{2}\right). \quad (7)$$

Consequently, both $\mathcal{N}_r(T_r,\varphi_r)$ and $E_{g,r}(T_r,\varphi_r)$ strongly depend on φ_r (at fixed T_r) and thus on the electronic temperature of the detection junction (while T_r is kept constant).

To maximize the responsivity of the detector, we implement the output tunnel probe p in the form of a superconducting wire. Indeed, SQUIPTs with superconducting tunnel probes show enhanced output signals [31,32]. Thus, the normalized DOS of p reads

$$\mathcal{N}_p(\varepsilon,V) = \left|\mathrm{Re}\left[\frac{(\varepsilon-eV+i\Gamma_p)}{\sqrt{(\varepsilon-eV+i\Gamma_p)^2-\Delta_p^2(T_p)}}\right]\right|, \quad (8)$$

where Γ_p is the Dynes parameter, Δ_p is the temperature-dependent superconducting energy gap, T_p is the electronic temperature, and V is the voltage drop across the tunnel barrier. The resulting quasiparticle tunnel current reads [25]

$$I(\varphi_r,V) = \frac{1}{ew_pR_p}\int_{\frac{\mathcal{L}_r-w_p}{2}}^{\frac{\mathcal{L}_r+w_p}{2}} dx \times \int_{-\infty}^{\infty} d\epsilon\, \mathcal{N}_r(x,\epsilon,\varphi_r)\mathcal{N}_p(\epsilon,V)\left[f_{0,p}(\epsilon-eV)-f_{0,r}(\varepsilon)\right], \quad (9)$$

where w_p is the width of p, R_p is the normal-state resistance of the $r-p$ tunnel junction, and $f_{0,r}$ and $f_{0,p}$ are the Fermi distributions of r and p, respectively. Equation (9) clearly shows that the output current is strongly dependent on φ_r and, thus, on the electron temperature of the detector T_d.

III. MATERIALS

In this section, we introduce the physical dimensions and the materials chosen for each element of the proposed nonlocal single-photon detector. In particular, we exploit a structure that is feasible using standard nanofabrication techniques. These structural features are employed to determine the detection performance of the device at a bath temperature $T_b = 10$ mK. The superconducting ring is assumed to be made of aluminum ($\Delta_0 = 200$ μeV). The detection and readout ring are assumed to show an inductance $L_d = 100$ pH and $L_r = 10$ pH, respectively. To ensure optimal interfaces and an efficient proximity effect, the S-N-S detector Josephson junction is made of copper (the DOS at the Fermi energy $N_{F,d} = 1.56 \times 10^{47}$ J^{-1}m^{-3} and diffusion constant $D_d = 10^{-2}$ m^{2}s^{-1})

with a length $\mathcal{L}_d = 1.5$ μm and a volume $\mathcal{V}_d = 12 \times 10^{-21}$ m^{-3}. Consequently, the normal-state resistance of d is $R_d = \rho_d \mathcal{L}_d^2/\mathcal{V}_d = \mathcal{L}_d^2/(e^2 N_{F,d} D_d \mathcal{V}_d) = 28\,\Omega$. Furthermore, the Thouless energy takes the value $E_{Th,d} = 2.93\ \mu\text{eV} \ll \Delta_0$; thus the junction lies in the long-limit regime. To ensure enough space for the output tunnel probe, the short-readout S-N-S Josephson junction is also made of copper. It is assumed to show a normal-state resistance $R_r = 500\,\Omega$ and a Dynes parameter $\Gamma_r = 10^{-4}\Delta_0$. In addition, the output probe (p) is made of aluminum ($\Delta_{0,p} = 200$ μeV and $\Gamma_p = 10^{-4}\Delta_{0,p}$) and is coupled to r by a tunnel connection of normal-state resistance $R_p = 10$ kΩ. Finally, the nonlocal detector can be realized on any substrate conventionally exploited for superconducting electronics, such as silicon, silicon dioxide, or sapphire. In particular, sapphire could be preferable due to its large phonon thermal conductance, thus ensuring efficient evacuation of the heat arising from the single-photon absorption.

IV. ENERGY-TO-TEMPERATURE CONVERSION

Here, we evaluate the increase of the temperature of the detector junction T_d due to the absorption of a photon of energy $h\nu$. We assume that a suitable antenna (e.g., bow tie, log-log dipole, or slit) funnels the energy of the single photons directly to d, since their direct absorption by d is limited by their long wavelength compared to the physical dimensions of the detection junction. The energy released by the single photons can be confined in the normal region of the detection junction by implementing Andreev mirrors (AMs) [33], which are superconducting elements with an energy gap larger than the ring ($\Delta_{0,AM} \gg \Delta_0$), thus preventing heat out-diffusion. Under this condition, the absorption of a photon exclusively causes the temperature of d to increase above the phonon temperature (T_b, i.e., the bath temperature). In particular, the temperature rises instantaneously up to a maximum value $T_{d,\text{peak}}$ and then electron-phonon (e-ph) collisions tend to restore equilibrium ($T_d = T_b$) [34]. Thus, we derive the dependence of $T_{d,\text{peak}}$ and the electron heat capacitance (C_d) on the frequency of the incident photon (ν). To this end, we introduce the temperature-dependent thermal capacitance of the normal state, defined as [18]

$$C_d(T_d) = \frac{\pi^2}{3}\mathcal{V}_d N_{F,d} k_B^2 T_d, \tag{10}$$

where $N_{F,d}$ is the DOS at the Fermi energy of d. We overestimate the thermal capacitance (and thus underestimate the temperature increase), since the presence of a superconducting minigap induced by the proximity effect damps C_d [35,36]. Moreover, the thermal capacitance in a long Josephson junction changes over the length of the normal-metal wire (since the minigap is position dependent) [37], thus complicating the analysis. We stress that our choice provides a simple solution without influencing the operation principle of the detector and providing an underestimated sensitivity. Within this model, the temperature $T_{d,\text{peak}}$ can be calculated by solving [38,39]

$$h\nu = \int_{T_b}^{T_{d,\text{peak}}} dT_d\ C_d = \frac{\pi^2}{6}\mathcal{V}_d N_{F,d} k_B^2 \left(T_{d,\text{peak}}^2 - T_b^2\right), \tag{11}$$

since the electron-electron thermalization is much faster than all the other energy exchange mechanisms in the system [17,34]. Indeed, the peak temperature takes the form

$$T_{d,\text{peak}}(\nu) = \sqrt{T_b^2 + \frac{6h\nu}{\pi^2 \mathcal{V}_d N_{F,d} k_B^2}}, \tag{12}$$

i.e., the peak temperature increases above T_b with the square root of the photon frequency. This behavior is shown in Fig. 1(b), where $T_{d,\text{peak}}$ is calculated as a function of ν at $T_b = 10$ mK. In particular, a single photon of frequency 10 GHz increases the electronic temperature of d to about 13 mK, while a 10-THz photon generates a $T_{d,\text{peak}} \simeq 260$ mK.

Finally, by substituting Eq. (12) in Eq. (10), we can compute the dependence of the thermal capacitance of d on the incident photon frequency:

$$\begin{aligned} C_{d,\text{peak}}(\nu) &= \frac{\pi^2}{3}\mathcal{V}_d N_{F,d} k_B^2 \sqrt{T_b^2 + \frac{6h\nu}{\pi^2 \mathcal{V}_d k_B^2}} \\ &= \pi k_B \sqrt{\frac{\mathcal{V}_d N_{F,d}}{3}\left(\frac{\pi^2 \mathcal{V}_d N_{F,d} k_B^2}{3} T_b^2 + 2h\nu\right)}. \end{aligned} \tag{13}$$

We stress that this is the value of the heat capacitance of d at the photon absorption; thus it depends on the square root of ν, as shown in the inset of Fig. 1(b). Indeed, in increasing ν by 3 orders of magnitude, the thermal capacitance rises by about a factor of 20.

V. ENERGY-TO-PHASE CONVERSION

Here, we evaluate the variations of φ_r due to absorption of a photon of frequency ν. To this end, we combine the temperature and phase dependence of the electronic transport of Josephson interferometers (see Sec. II) with the energy-to-temperature conversion mechanism in d (see Sec. IV).

At a given value of T_b and Φ_d, the absorption of a photon generates a change of the phase bias of r, given by

$$\varphi_r(\nu) = \frac{2\pi}{\Phi_0}\left[\Phi_d - L_d I_{C,d}(\nu)\sin\left(\varphi_r + 2\pi\frac{L_r I_r(T_b,\varphi_r)}{\Phi_0}\right) - (L_d + L_r) I_r(T_b,\varphi_r)\right], \quad (14)$$

where the readout junction is always fully thermalized with the phonon bath [i.e., $I_r(T_b,\varphi_r)$], while the critical current of d strongly depends on the frequency of the absorbed single photon

$$I_{C,d}(\nu) = \frac{\sqrt{4096\pi^2 k_B^2 T_b^2 + \frac{24576h\nu}{\gamma_d N_{F,d}}}}{(3+2\sqrt{2})eR_d} \times \sqrt[4]{\frac{4\pi^2 k_B^2 T_b^2 + \frac{24h\nu}{\gamma_d N_{F,d}}}{E_{\mathrm{th},d}^2}} \times \exp\left(-\sqrt[4]{\frac{4\pi^2 k_B^2 T_b^2 + \frac{24h\nu}{\gamma_d N_{F,d}}}{E_{\mathrm{th},d}^2}}\right). \quad (15)$$

As a consequence, φ_r is predicted to show a strong dependence on the incident photon frequency. The details of the calculations for deriving Eqs. (14) and (15) are provided in Appendix A.

Figure 2(a) shows the dependence of the phase drop across the readout junction on the photon frequency for different values of Φ_d. In particular, the variation of φ_r with ν increases with the flux bias, approaching its maximum for $\Phi_d \to 0.5\Phi_0$. Indeed, the detector shows $\delta\varphi_r(\Phi_d = 0.01\Phi_0) = |\varphi_r(0.01\Phi_0, 10\ \mathrm{GHz}) - \varphi_r(0.01\Phi_0, 10\ \mathrm{THz})| \simeq 5.7\times10^{-3}\pi$ and $\delta\varphi_r(\Phi_d = 0.49\ \Phi_0) \simeq 0.29\pi$. Interestingly, the phase starts to vary at lower frequencies by increasing Φ_d, thus suggesting a larger sensitivity of the single-photon detector. In the same flux range, φ_d reaches values larger than $\pi/2$. This implies that the value of Φ_d determines whether the photon absorption causes an increase or decrease of the induced minigap of r [see Eq. (7)]. Figure 2(b) shows the dependence of the induced minigap $E_{g,r}$ on ν for different values of the flux bias. The minigap increases monotonically for $\Phi_d \leq 0.3\Phi_0$, while $E_{g,r}$ is damped for $\Phi_d = 0.49\Phi_0$ (gray curve). On the other hand, the minigap shows a nonmonotonic dependence on ν for $\Phi_d = 0.4\Phi_0$. In fact, in this case, φ_r crosses $\pi/2$ [see Fig. 2(a)], which defines the periodicity of $E_{g,r}(\varphi_r)$. Consequently, the choice of a specific value of Φ_d defines the sensitivity of the system to the absorption of single photons of different energy.

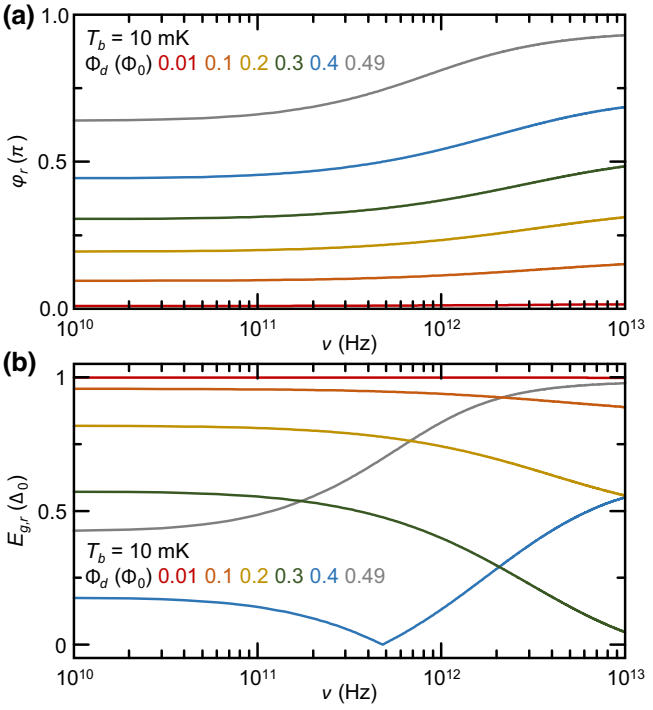

FIG. 2. (a) The superconducting phase drop across the readout junction (φ_r) versus the frequency of the incident photon (ν), calculated for different values of the magnetic flux biasing the device (Φ_d). (b) The superconducting minigap induced in r ($E_{g,r}$) versus ν, calculated for different values of Φ_d. All calculations are performed at $T_b = 10$ mK.

VI. OUTPUT CURRENT VERSUS ν

In this section, we evaluate the influence of the single-photon absorption on the quasiparticle transport of the nonlocal detector. Indeed, the energy-to-phase conversion implies a frequency-dependent change of the DOS of r [see Eq. (6)] and thus a modification of the detector output signal [see Eq. (9)].

Figure 3(a) shows the quasiparticle current (I) versus voltage (V) characteristics of the detector calculated by solving Eq. (9) at $T_b = 10$ mK and $\Phi_d = 0.49\Phi_0$. In particular, we evaluate the difference between the response in the absence of radiation ($\nu = 0$, black) and in the presence of a single photon of frequency $\nu = 10$ THz (gray) by exploiting Eqs. (6), (14), and (15) to evaluate φ_r. The I-V curves show the typical behavior of a tunnel junction between two superconductors, where the current increases dramatically at the transition to the normal state ($V \sim [\Delta_p(T_b) + E_{g,r}(\varphi_r)]/e$). As shown in Fig. 2(b), at $\Phi_d = 0.49\Phi_d$, the absorption of a photon causes the increase of the induced minigap in r. Thus, the transition to the normal-state behavior of the I-V characteristics moves toward larger values of the bias voltage after photon absorption. This feature is combined with a change in the conduction of the subgap quasiparticles. Therefore,

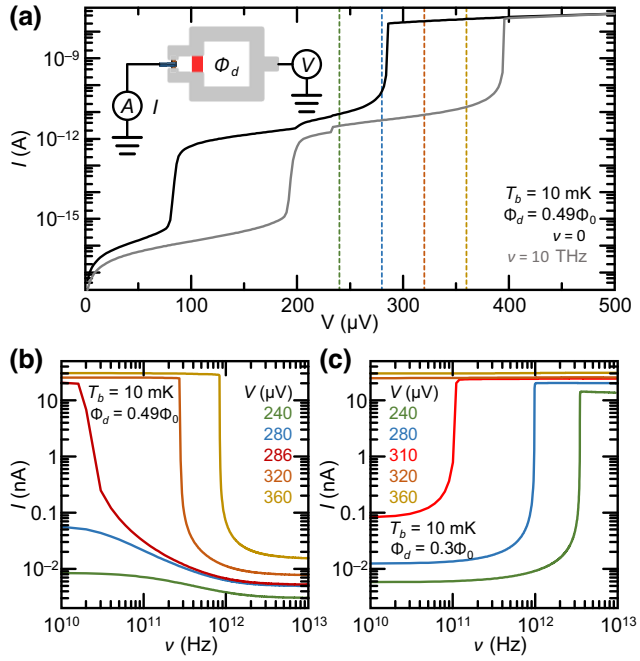

FIG. 3. (a) The current (I) versus voltage (V) characteristics of the nonlocal single-photon detector in the absence of incident radiation (gray) and for an incident photon of frequency $\nu = 10$ THz, calculated at $\Phi_d = 0.49\Phi_0$. The dashed vertical lines indicate suitable values of the bias voltage for the device operation. The inset shows the readout scheme of the detector, where Φ_d is the bias flux, V is the bias voltage, and I is the measured quasiparticle tunnel current. (b) I versus ν calculated for different values of V at $\Phi_d = 0.49\Phi_0$. $V = 286$ μV (red) is the bias that ensures current modulation at lower frequency. (c) I versus ν calculated for different values of V at $\Phi_d = 0.3\Phi_0$. $V = 310$ μV (red) is the bias that ensures current modulation at lower frequency. All calculations are performed at $T_b = 10$ mK.

we can measure the absorption of a single photon by recording the tunnel current at a fixed V [see the inset of Fig. 3(a)]. In general, the appropriate bias voltages lie in the range $\Delta_0 \leq eV \leq 2\Delta_0$, since $\Delta_p(10\ \text{mK}) \sim \Delta_0$ and $0 \leq E_{g,r}(\varphi_0) \leq \Delta_0$. In our setting, the voltage bias range is thus 200 μV $\leq V \leq$ 400 μV. This allows us to generate easily measurable modulations of I. Despite I also being modulated for $eV < \Delta_0$ ($V < 200$ μV), the absolute value of the current is rather small and thus impractical in concrete experimental setups. Indeed, we choose four values of V in the best bias range to determine the current output and the performance of the nonlocal single-photon detector [see dashed lines in Fig. 3(a)].

We first focus on the modulation of I for values of the magnetic flux bias guaranteeing a monotonic dependence of $E_{g,r}$ on ν (increasing or decreasing). Accordingly, the quasiparticle current tends to decrease after the photon absorption for $\Phi_d = 0.49\Phi_0$ [Fig. 3(b)], while I rises for $\Phi_d = 0.3\Phi_0$ [Fig. 3(c)]. In other words, the output signal depends (increases or decreases) monotonically on the energy of the incident photon. Beyond the voltage values shown in Fig. 3(a), we include the $I(\nu)$ characteristics calculated for the values of V that ensure the onset of the current variation at the lowest photon frequency (red lines). In particular, the highest current modulation is ensured for $V = 286$ μV at $\Phi_d = 0.49\Phi_0$ and for $V = 310$ μV at $\Phi_d = 0.3\Phi_0$. At $\Phi_d = 0.49\Phi_0$, the current starts to vary over several orders of magnitude, starting from $\nu \simeq 20$ GHz, while for a flux bias $\Phi_d = 0.3\Phi_0$, the strong I increase happens around 70 GHz. This behavior is a direct consequence of the $E_{g,r}(\nu)$ characteristics shown in Fig. 2(b) and suggests sensitivity of the detector also at those low frequencies.

We now switch our attention to $\Phi_d = 0.4\Phi_0$, where the $E_{g,r}(\nu)$ characteristics are nonmonotonic. Thus, we expect a richer and more complex behavior of the detector output current. Indeed, the sign of the derivative of I changes with increasing ν [see Eq. (9)]. For $V \geq 240$ μV, the current decreases monotonically with the radiation frequency [see Fig. 4(a)], since the $E_{g,r}(\nu)$ characteristics are single valued and monotonically increasing with ν at the energies corresponding to these values of V, as shown by the blue curve in Fig. 2(b). On the other hand, for lower values of the bias voltage, $E_{g,r}(\nu)$ is nonmonotonic, since the phase drop φ_r crosses the symmetry point at 0.5π [see Fig. 2(a)]. Thus, the system provides two possible values of ν at a given V. Consequently, the $I(\nu)$ characteristics are nonmonotonic for $V < 240$ μV. In particular, the current increases at low frequencies, stays constant for about a decade in frequency, and starts to decrease again at larger values of ν [see Fig. 4(b)]. On the one hand, the onset of the I dampening is weakly dependent on V (from approximately 1 THz at $V = 220$ μV to approximately 2 THz at $V = 240$ μV). On the other, the onset of the current increases can be tuned over more than one order of magnitude by changing the bias voltage in the same range. In particular, by setting $V = 234$ μV, the current is already sensitive for 10-GHz single photons, while $V = 220$ μV provides a strong current modulation at about 200 GHz. Consequently, the choice of the flux Φ_d and the bias voltage V allows us to determine the sign of the current variation with photon absorption and to choose the sensitivity frequency range. In particular, the device acts an energy-proportional detector by setting the right value of Φ_d, as shown in Figs. 3(b) and 3(c).

The nonlocal detector can be exploited to design cameras, with the possibility of addressing more pixels due to frequency-domain multiplexing. Indeed, in full analogy with TESs [1,3–6], the device produces an output current at a constant voltage bias (change of resistance). Thus, each pixel can be inserted in an *RLC* circuit of a specific resonance frequency that changes the transmitted signal intensity at the photon absorption [7]. Finally, all the different tones can be amplified by a superconducting quantum interference device (SQUID) amplifier that is inductively coupled to the detector array.

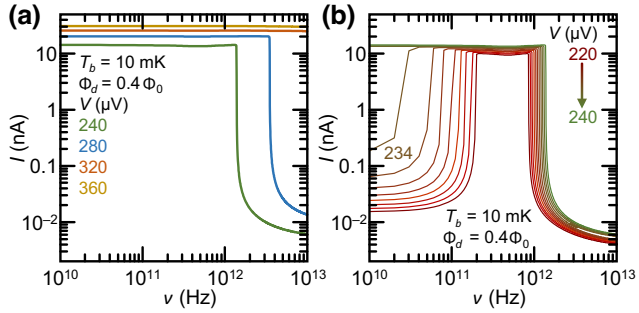

FIG. 4. (a) I versus ν calculated for different values of the bias voltage (V). (b) I versus ν calculated for values V that highlight the nonmonotonic modulation of $E_{g,r}$ with increasing incident photon frequency. All calculations are performed at $\Phi_d = 0.4\Phi_0$ and $T_b = 10$ mK.

VII. SINGLE-PHOTON-DETECTION PERFORMANCE

Here, we investigate the sensitivity of our nonlocal single-photon detector by calculating the typical figures of merit for a calorimeter, such as the signal-to-noise ratio (SNR), the energy resolution ($h\nu/\delta E$), and the time constant ($\tau_{1/2}$). We note that for a superconducting detector (and thus for the proposed device), the simultaneous absorption of two photons is equivalent to the absorption of a single photon of energy equal to the sum of the two photons.

The signal-to-noise ratio evaluates the magnitude of the signal produced by the detector when sensing a single photon with respect to the background noise. In voltage bias, the SNR reads

$$\mathrm{SNR}\ (\nu) = \frac{|I[V,\varphi_r(\nu)] - I[V,\varphi_r(\nu=0)]|}{\sqrt{S_{I,\mathrm{tot}}}\sqrt{\omega}}, \qquad (16)$$

where $S_{I,\mathrm{tot}}$ is the total current-noise spectral density (see Appendix B for details) and $\omega = 1$ MHz is the measurement bandwidth. This choice satisfies the requirement $\omega \geq 2\pi/\tau_{1/2}$, where $\tau_{1/2}$ is the characteristic time constant of the detector (as calculated below).

Figure 5 shows the dependence of the SNR on the photon frequency calculated at the same values of Φ_d and V selected for the $I(\nu)$ characteristics (see Sec. VI). In particular, Fig. 5(a) shows the SNR (ν) characteristics calculated for $\Phi_d = 0.49\Phi_0$. As expected for this flux bias, the SNR increases monotonically with the photon frequency. In addition, the detector is sensitive to low-frequency single photons in these conditions of the flux and voltage bias, showing the larger change of the probe current. Indeed, the detector is able detect single photons of frequency approximately 10 GHz (SNR > 1) for $V = 286$ μV with maximum values of the signal-to-noise ratio of about 255 at $\nu = 10$ THz. Similarly, Fig. 5(b) shows the SNR (ν) characteristics obtained for $\Phi_d = 0.3\Phi_0$. On the

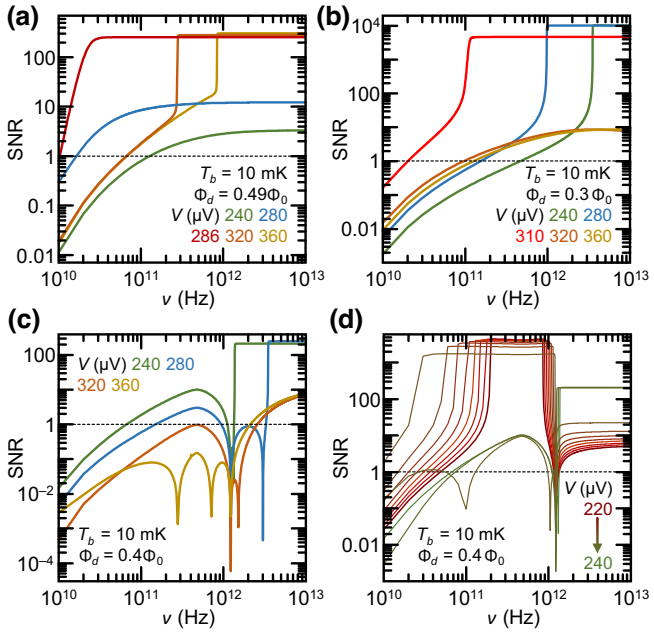

FIG. 5. (a)–(c) The signal-to-noise ratio (SNR) versus the photon frequency (ν) calculated for different values of the bias voltage (V) at (a) $\Phi_d = 0.49\Phi_0$, (b) $\Phi_d = 0.3\Phi_0$, and (c) $\Phi_d = 0.4\Phi_0$. (d) SNR versus ν calculated for values of the voltage (V) around the maximum sensitivity at $\Phi_d = 0.4\Phi_0$. The dashed lines indicate the lower limit for single-photon detection (SNR $= 1$). All curves are calculated for $T_b = 10$ mK.

one hand, the detector is less sensitive to low-frequency photons (SNR ≥ 1 for $\nu \gtrsim 20$ GHz at $V = 310$ μV). On the other, the detector reaches SNR $\sim 10^4$ at 10 THz for $V = 240$ μV, since the output current increases when absorbing a single photon, thus providing a signal much larger than the dark-current noise ($\nu = 0$).

Differently, the SNR is nonmonotonic with the frequency at $\Phi = 0.4\Phi_0$ [see Figs. 5(c) and 5(d)], thus reflecting the behavior of the $I(\nu)$ characteristics. Interestingly, the detector is insensitive to low-frequency photons for a wide range of bias voltages (SNR > 1 for $\nu \gtrsim 2.5$ THz for $V = 360$ μV). In the optimally biased case [$V = 234$ μV, Fig. 5(d)], the detector is able to reveal 10-GHz single photons but it becomes blind for frequencies $\nu \sim 1$ THz. Therefore, the bias voltage can be exploited to tune the sensitivity of the detector to single photons of the desired energy while *filtering* part of the remaining electromagnetic spectrum. We note that the sensitivity of the detector to photons of extremely low frequency (down to 10 GHz) highlights the importance of the proposed nonlocal readout mechanism. Indeed, low dissipated power into the detector junction due to direct tunnel measurements or even the quasiparticles created by dispersive measurements can affect the detector response. As a consequence, these effects can decrease the effective sensitivity of the detector by increasing the noise levels and the dark counts.

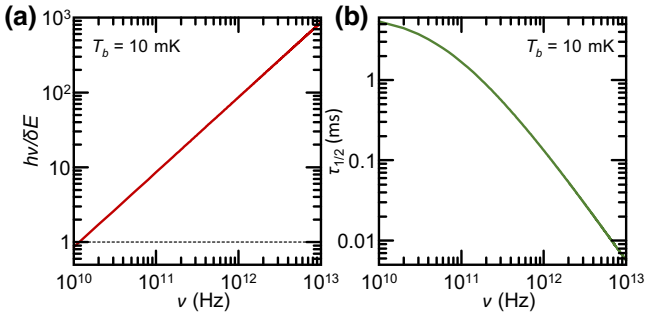

FIG. 6. (a) The energy resolution ($h\nu/\delta E$) versus the photon frequency (ν). The dashed line indicates $h\nu/\delta E = 1$. (b) The time constant ($\tau_{1/2}$) versus ν. All curves are calculated at $T_b = 10$ mK.

The energy resolution describes the ability of a detector to distinguish the energy of the revealed single photon. For the proposed device, it can be evaluated through

$$\frac{h\nu}{\delta E}(\nu, T_b) = \frac{h\nu}{4\sqrt{2\ln 2\, k_B T_b^2 C_d(T_d = T_b)}}, \qquad (17)$$

where the thermal capacitance C_d is evaluated at T_b, i.e., at the temperature of d before the photon absorption. Figure 6(a) shows $h\nu/\delta E$ for our nonlocal detector calculated at $T_b = 10$ mK. In particular, the sensor can discern single photons of energy approximately 10 GHz ($h\nu/\delta E \geq 1$). Moreover, the detector shows an energy resolution of about 10^3 for 10-THz single photons. We stress that we exploit the normal-state thermal capacitance [see Eq. (10)], thus underestimating the energy resolution. This underestimation is larger for low energies, where the overheating is lower and the difference between the value of C_d in the superconducting and normal state is at a maximum [35,36]. Therefore, these are low boundary values of the energy resolution.

Finally, the characteristic time constant of our single-photon detector can be determined by considering only half of the e-ph relaxation time ($\tau_{1/2}$), i.e., the time necessary to have $T_d = (T_b + T_{d,\mathrm{peak}})/2$, since the time response of the output tunnel probe is much faster than the energy diffusion. In particular, $\tau_{1/2}$ is defined as follows:

$$\tau_{1/2} = \int_{(T_b+T_{d,\mathrm{peak}})/2}^{T_{d,\mathrm{peak}}} dT_d\, \frac{C_d(T_d)}{P_{e,ph}(T_d, T_b)}, \qquad (18)$$

where $P_{e,ph} = \mathcal{V}_d \Sigma_d (T_d^5 - T_b^5)$ (in which $\Sigma_d = 2 \times 10^9$ $\mathrm{Wm^{-3}K^{-5}}$ is the e-ph coupling constant of copper) is the e-ph thermalization in d [34]. We note that to be consistent with the heat capacitance, we consider the e-ph thermalization in the normal state. In our device, the characteristic time of the detector decreases by increasing ν [see Fig. 6(b)] from approximately 6 ms at 10 GHz to approximately 70 μs at 10 THz. This is due to the rise of the e-ph thermalization at the large electronic temperatures, as reached at high single-photon frequency. In addition, we point out that the thermalization is dominated by the e-ph scattering even in the absence of AMs, since an aluminum thin film is almost completely thermally insulating up to electronic temperatures of about 280 mK [7] (which is larger than the $T_{d,\mathrm{peak}} \simeq 270$ mK reached for 10-THz single photons). The time scale defined by $\tau_{1/2}$ represents the jitter of the detector, since the change of the electronic temperature limits the operation speed and the ability to measure two consequent incoming photons. In fact, the energy of two consequent photons can be determined only when their time separation is large enough to ensure the full recovery of the electronic temperature of d to T_b; otherwise, the device can only operate as a photon counter, with no energy discrimination. Furthermore, a large number of absorbed photons before the rethermalization could bring the system to the normal state, thus impeding the response of the detector.

VIII. CONCLUSIONS

In summary, we propose a nonlocal superconducting single-photon detector that operates due to the *energy-to-phase* conversion mechanism. The device is composed of a double-loop interferometer with a long S-N-S Josephson junction acting as detector and a short S-N-S operating as readout. The device output signal is the quasiparticle current recorded by a superconducting electrode tunnel coupled directly to the readout junction. Despite the complex design, the separation of the detection and readout elements ensures improved sensitivity and suppressed electronic noise arising from the measurement operations. Differently from previous nonlocal detectors, our analysis takes into account the nonideal phase bias due to the finite kinetic inductance of the superconducting loops composing the device. By exploiting an experimentally feasible structure and materials, the proposed detector is able to reveal single photons of frequency down to 10 GHz with an energy resolution larger than 1 when operated at 10 mK. Furthermore, the sensitivity can be tuned by controlling the magnetic flux piercing the detection loop and the bias voltage. In particular, the response to single photons in specific windows of the electromagnetic range could be filtered by setting the biasing parameters. Since the large detector sensitivity arises from the exponential temperature dependence of the critical current of the long–S-N-S–detector Josephson junction, the use of large critical-temperature materials (such as Nb or NbN) could allow us to increase the operation temperature. In these systems, the detection sensitivity could be limited slightly by the increase of the e-ph thermalization at higher phonon temperatures and the realization of the tunnel output on the short-readout junction could be impractical due to the short coherence length that characterizes these higher-T_C superconductors.

This single-photon detector can find applications in both quantum technologies and basic science, such as quantum cryptography [40,41], optical quantum computing [42], terahertz spectroscopy [43], and particle search [44]. Furthermore, the nonlocal and noninvasive detection scheme might also be exploited for the readout [45] or memory [46] operations of superconducting qubits.

ACKNOWLEDGMENTS

I thank G. Lamanna, S. Roddaro, G. Signorelli, P. Spagnolo, A. Tartari, and A. Tredicucci for fruitful discussions. The author acknowledge F. Bianco for critically reading the manuscript.

I declare no competing financial interest.

APPENDIX A: CALCULATION OF φ_r VERSUS ν

Here, we derive the dependence of the superconducting phase drop across the readout junction (φ_r) on the frequency of the incident photon (ν). Within this scope, we need to consider the fluxoid quantization of the detection loop [19],

$$\varphi_d + \frac{2\pi L_d}{\Phi_0} I_{\rm tot} = 2\pi \frac{\Phi_d}{\Phi_0}, \tag{A1}$$

the fluxoid quantization of the readout loop (assuming that $\Phi_r = 0$),

$$\varphi_r - \varphi_d + \frac{2\pi L_r}{\Phi_0} I_r = 0, \tag{A2}$$

and the conservation of the circulating current,

$$I_{\rm tot} = I_d + I_r. \tag{A3}$$

We can extract φ_r by combining Eqs. (A1) and (A2):

$$\begin{aligned}\varphi_r &= \varphi_d - 2\pi \frac{L_r I_r}{\Phi_0} \\ &= 2\pi \frac{\Phi_d}{\Phi_0} - 2\pi \frac{L_d I_{\rm tot}}{\Phi_0} - 2\pi \frac{L_r I_r}{\Phi_0} \\ &= \frac{2\pi}{\Phi_0}\left[\Phi_d - L_d I_{\rm tot} - L_r I_r\right].\end{aligned} \tag{A4}$$

By substituting the circulating-current conservation [Eq. (A3)], the phase drop can be written as

$$\begin{aligned}\varphi_r &= \frac{2\pi}{\Phi_0}\left[\Phi_d - L_d(I_d + I_r) - L_r I_r\right] \\ &= \frac{2\pi}{\Phi_0}\left[\Phi_d - L_d I_d - L_d I_r - L_r I_r\right] \\ &= \frac{2\pi}{\Phi_0}\left[\Phi_d - L_d I_d - I_r(L_d + L_r)\right].\end{aligned} \tag{A5}$$

We now simplify φ_d and introduce the dependence of I_d on the temperature. To this end, we introduce the expression for the switching current of d (long S-N-S Josephson junction),

$$I_d(T_d, \varphi_d) = I_{C,d}(T_d)\sin(\varphi_d), \tag{A6}$$

and substitute

$$\varphi_d = \varphi_r + 2\pi \frac{L_r I_r(T_r, \varphi_r)}{\Phi_0}. \tag{A7}$$

As a consequence, at a given value of Φ_d, the phase drop across r depends strongly on both T_d and T_r, as shown by

$$\begin{aligned}&\varphi_r(T_d, T_r) \\ &= \frac{2\pi}{\Phi_0}\left[\Phi_d - L_d I_{C,d}(T_d)\sin(\varphi_d) - (L_d + L_r) I_r(T_r, \varphi_r)\right] \\ &= \frac{2\pi}{\Phi_0}\left[\Phi_d - L_d I_{C,d}(T_d)\sin\left(\varphi_r + 2\pi \frac{L_r I_r(T_r, \varphi_r)}{\Phi_0}\right)\right. \\ &\left. - (L_d + L_r) I_r(T_r, \varphi_r)\right].\end{aligned} \tag{A8}$$

We note that φ_r has an exponential dependence on $\sqrt{T_d}$, since $I_{C,d} \propto \exp(-\sqrt{T_d})$ for a Josephson junction in the long-diffusion limit [see Eq. (2)] [22,23]. The absorption of a photon increases the temperature of d above T_b [see Eq. (12) and Fig. 1(b)] up to the maximum value $T_{d,\rm peak}$ (see Sec. IV), while it does not affect the readout-junction temperature ($T_r = T_b$). Therefore, at a given T_b and Φ_d, φ_r is only a function of ν, as shown by

$$\begin{aligned}&\varphi_r(\nu, T_b) \\ &= \frac{2\pi}{\Phi_0}\left[\Phi_d - L_d I_{C,d}(\nu)\sin\left(\varphi_r + 2\pi \frac{L_r I_r(T_b, \varphi_r)}{\Phi_0}\right)\right. \\ &\left. - (L_d + L_r) I_r(T_b, \varphi_r)\right].\end{aligned} \tag{A9}$$

Finally, by substituting Eq. (12) into Eq. (2), we obtain the dependence of the critical current of d on the photon frequency [Eq. (15)]:

$$\begin{aligned}I_{C,d}(\nu) = &\frac{\sqrt{4096\pi^2 k_B^2 T_b^2 + \frac{24576 h\nu}{\gamma_d N_{F,d}}}}{(3 + 2\sqrt{2}) e R_d} \\ &\times \sqrt[4]{\frac{4\pi^2 k_B^2 T_b^2 + \frac{24 h\nu}{\gamma_d N_{F,d}}}{E_{{\rm th},d}^2}} \\ &\times \exp\left(-\sqrt[4]{\frac{4\pi^2 k_B^2 T_b^2 + \frac{24 h\nu}{\gamma_d N_{F,d}}}{E_{{\rm th},d}^2}}\right).\end{aligned} \tag{A10}$$

Small fluctuations of T_b have limited impact on φ_r, since the e-ph thermalization is strongly suppressed in nanoscale

metallic systems (in superconducting thin films the *e*-ph scattering is exponentially suppressed by the superconducting energy gap) [34].

APPENDIX B: CURRENT-NOISE SPECTRAL DENSITY

The total current-noise spectral density takes the form

$$S_{I,\mathrm{tot}} = S_{I,TFN} + S_{I,p}, \tag{B1}$$

where $S_{I,TFN}$ is the current noise related to the thermal fluctuations in the detector and $S_{I,p}$ is the low-frequency current-noise of p calculated in the idle state (i.e., in the absence of radiation).

The thermal fluctuation noise can be calculated by [17]

$$S_{I,TFN} \simeq \frac{|I[V=0,\varphi_r(\nu)] - I[V=0,\varphi_r(\nu=0)]|^2}{\omega}, \tag{B2}$$

which is related to the different between the current fluctuations in the presence and in the absence of radiation when no voltage bias is applied.

The current noise of the probe takes the form

$$S_{I,p} = 2eI[V,\varphi_r(\nu=0)]\coth\left(\frac{eV}{2k_BT_b}\right), \tag{B3}$$

which is the intrinsic noise of the tunnel probe at voltage V and temperature T_b, i.e., in a dark environment.

[1] K. D. Irwin, An application of electrothermal feedback for high resolution cryogenic particle detection, Appl. Phys. Lett. **66**, 1998 (1995).

[2] P. K. Day, H. G. LeDuc, B. A. Mazin, A. Vayonakis, and J. Zmuidzinas, A broadband superconducting detector suitable for use in large arrays, Nature **425**, 817 (2003).

[3] T. Suzuki, P. Khosropanah, R. A. Hijmering, M. Ridder, M. Schoemans, H. Hoevers, and J. R. Gao, Performance of SAFARI short-wavelength-band transition edge sensors (TES) fabricated by deep reactive ion etching, IEEE Trans. THz Sci. Technol. **4**, 171 (2014).

[4] P. J. de Visser, J. J. A. Baselmans, J. Bueno, N. Llombart, and T. M. Klapwijk, Fluctuations in the electron system of a superconductor exposed to a photon flux, Nat. Commun. **5**, 3130 (2014).

[5] K. Niwa, T. Numata, K. Hattori, and D. Fukuda, Few-photon color imaging using energy-dispersive superconducting transition-edge sensor spectrometry, Sci. Rep. **7**, 45660 (2017).

[6] A. Elefante, S. Dello Russo, F. Sgobba, L. Santamaria Amato, D. K. Pallotti, D. Dequal, and M. Siciliani de Cumis, Recent progress in short and mid-infrared single-photon generation: A review, Optics **4**, 13 (2023).

[7] F. Paolucci, V. Buccheri, G. Germanese, N. Ligato, R. Paoletti, G. Signorelli, M. Bitossi, P. Spagnolo, P. Falferi, M. Rajteri, C. Gatti, and F. Giazotto, Development of highly sensitive nanoscale transition edge sensors for gigahertz astronomy and dark matter search, J. Appl. Phys. **128**, 194502 (2020).

[8] C. M. Natarajan, M. G. Tenner, and R. H. Hadfield, Superconducting nanowire single-photon detectors: Physics and applications, Supercond. Sci. Technol. **25**, 063001 (2012).

[9] L. You, Superconducting nanowire single-photon detectors for quantum information, Nanophotonics **9**, 2673 (2020).

[10] G. Oelsner, L. S. Revin, E. Il'ichev, A. L. Pankratov, H.-G. Meyer, L. Grönberg, J. Hassel, and L. S. Kuzmin, Underdamped Josephson junction as a switching current detector, Appl. Phys. Lett. **103**, 142605 (2013).

[11] C. Guarcello, A. Braggio, P. Solinas, G. P. Pepe, and F. Giazotto, Josephson-Threshold Calorimeter, Phys. Rev. Appl. **11**, 054074 (2019).

[12] F. Giazotto, T. T. Heikkilä, G. P. Pepe, P. Helistö, A. Luukanen, and J. P. Pekola, Ultrasensitive proximity Josephson sensor with kinetic inductance readout, Appl. Phys. Lett. **92**, 162507 (2008).

[13] R. Kokkoniemi, J. Govenius, V. Vesterinen, R. E. Lake, A. M. Gunyhó, K. Y. Tan, S. Simbierowicz, L. Grönberg, J. Lehtinen, M. Prunnila, and J. Hassel, Nanobolometer with ultralow noise equivalent power, Commun. Phys. **2**, 124 (2019).

[14] T. T. Heikkilä, O. Ojajärvi, I. J. Maasilta, E. Strambini, F. Giazotto, and F. S. Bergeret, Thermoelectric Radiation Detector Based on Superconductor-Ferromagnet Systems, Phys. Rev. Appl. **10**, 034053 (2018).

[15] F. Paolucci, G. Germanese, A. Braggio, and F. Giazotto, A highly-sensitive broadband superconducting thermoelectric single-photon detector, Appl. Phys. Lett. **122**, 173503 (2023).

[16] F. Paolucci, N. Ligato, V. Buccheri, G. Germanese, P. Virtanen, and F. Giazotto, Hypersensitive Tunable Josephson Escape Sensor for Gigahertz Astronomy, Phys. Rev. Appl. **14**, 034055 (2020).

[17] P. Virtanen, A. Ronzani, and F. Giazotto, Josephson Photodetectors via Temperature-to-Phase Conversion, Phys. Rev. Appl. **9**, 054027 (2018).

[18] P. Solinas, F. Giazotto, and G. P. Pepe, Proximity SQUID Single-Photon Detector via Temperature-to-Voltage Conversion, Phys. Rev. Appl. **10**, 024015 (2018).

[19] J. Clarke and J. Bragisnki, *The SQUID Handbook* (VCH, New York, 2004).

[20] F. Paolucci, P. Solinas, and F. Giazotto, Inductive Superconducting Quantum Interference Proximity Transistor: The L-SQUIPT, Phys. Rev. Appl. **18**, 054042 (2022).

[21] A. A. Golubov, M. Yu. Kupriyanov, and E. Il'Chev, The current-phase relation in Josephson junctions, Rev. Mod. Phys. **76**, 411 (2004).

[22] A. D. Zaikin and G. F. Zharkov, Effect of external fields and impurities on the Josephson current in SNINS junctions, Sov. J. Low Temp. Phys. **7**, 184 (1981).

[23] F. K. Wilhelm, A. D. Zaikin, and G. Schön, Supercurrent in a mesoscopic proximity wire, J. Low Temp. Phys. **106**, 305 (1997).

[24] F. Giazotto, J. T. Peltonen, M. Meschke, and J. P. Pekola, Superconducting quantum interference proximity transistor, Nat. Phys. **6**, 254 (2010).

[25] F. Giazotto and F. Taddei, Hybrid superconducting quantum magnetometer, Phys. Rev. B **84**, 214502 (2011).
[26] I. O. Kulik and A. N. Omel'yanchuk, Contribution to the microscopic theory of the Josephson effect in superconducting bridges, JEPT Lett. **21**, 96 (1975).
[27] S. N. Artemenko, A. F. Volkov, and A. V. Zaitsev, Theory of nonstationary Josephson effect in short superconducting contacts, Sov. Phys. JEPT **49**, 924 (1979).
[28] T. T. Heikkilä, J. Särkkä, and F. K. Wilhelm, Supercurrent carrying density of states in diffusive mesoscopic Josephson weak links, Phys. Rev. B **66**, 184513 (2002).
[29] R. C. Dynes, J. P. Garno, G. B. Hertel, and T. P. Orlando, Tunneling Study of Superconductivity near the Metal-Insulator Transition, Phys. Rev. Lett. **53**, 2437 (1984).
[30] P. G. De Gennes, *Superconductivity of Metals and Alloys*, Advanced Book Classics (Perseus, Cambridge, Massachusetts, 1999).
[31] R. N. Jabdaraghi, M. Meschke, and J. P. Pekola, Non-hysteretic superconducting quantum interference proximity transistor with enhanced responsivity, Appl. Phys. Lett. **104**, 082601 (2014).
[32] P. Virtanen, A. Ronzani, and F. Giazotto, Spectral Characteristics of a Fully Superconducting SQUIPT, Phys. Rev. Appl. **6**, 054002 (2016).
[33] A. F. Andreev, The Thermal Conductivity of the Intermediate State in Superconductors, JEPT **66**, 1228 (1964).
[34] F. Giazotto, T. T. Heikkilä, A. Luukanen, A. M. Savin, and J. P. Pekola, Opportunities for mesoscopics in thermometry and refrigeration: Physics and applications, Rev. Mod. Phys. **78**, 217 (2006).
[35] H. Rabani, F. Taddei, O. Bourgeois, R. Fazio, and F. Giazotto, Phase-dependent electronic specific heat of mesoscopic Josephson junctions, Phys. Rev. B **78**, 012503 (2008).
[36] H. Rabani, F. Taddei, F. Giazotto, and R. Fazio, Influence of interface transmissivity and inelastic scattering on the electronic entropy and specific heat of diffusive superconductor-normal metal-superconductor Josephson junctions, J. Appl. Phys. **105**, 093904 (2009).
[37] H. le Sueur, P. Joyez, H. Pothier, C. Urbina, and D. Esteve, Phase Controlled Superconducting Proximity Effect Probed by Tunneling Spectroscopy, Phys. Rev. Lett. **100**, 197002 (2008).
[38] S. H. Moseley, J. C. Mather, and D. McCammon, Thermal detectors as x-ray spectrometers, J. Appl. Phys. **67**, 1257 (1984).
[39] T. C. P. Chui, D. R. Swanson, M. J. Adriaans, J. A. Nissen, and J. A. Lipa, Temperature Fluctuations in the Canonical Ensemble, Phys. Rev. Lett. **69**, 3005 (1992).
[40] N. Gisin, G. Ribordy, W. Tittel, and H. Zbiden, Quantum cryptography, Rev. Mod. Phys. **74**, 145 (2002).
[41] W. Tittel, Quantum key distribution breaking limits, Nat. Photon. **13**, 310 (2019).
[42] J. L. O'brien, Optical quantum computing, Science **318**, 1567 (2007).
[43] K.-E. Peiponen, A. Zeitler, and M. Kuwata-Gonokami, *Terahertz Spectroscopy and Imaging* (Springer, Berlin, 2013).
[44] P. Sikivie, Experimental Tests of the Invisible Axion, Phys. Rev. Lett. **51**, 1415 (1983).
[45] I. Siddiqi, Engineering high-coherence superconducting qubits, Nat. Rev. Mater. **6**, 875 (2021).
[46] N. Ligato, E. Strambini, F. Paolucci, and F. Giazotto, Preliminary demonstration of a persistent Josephson phase-slip memory cell with topological protection, Nat. Commun. **12**, 5200 (2021).